

Microscopic quantum description of second-order nonlinearities in 2D hexagonal nanostructures beyond the Dirac cone approximation

H.K. Avetissian¹, G.F. Mkrtchian¹, K.G. Batrakov², S.A. Maksimenko²

¹ *Centre of Strong Fields Physics, Yerevan State University, 0025 Yerevan, Armenia,*

² *Institute for Nuclear Problems, Belarusian State University, 220050 Minsk, Belarus*

(Dated: May 30, 2022)

Single layers of hexagonal two-dimensional nanostructures such as graphene, silicene, and germanene exhibit large carrier Fermi velocities and, consequently, large light-matter coupling strength making these materials promising elements for nano-opto-electronics. Although these materials are centrosymmetric, the spatial dispersion turns out to be quite large allowing the second-order nonlinear response of such materials to be comparable to the non-centrosymmetric 2D ones. The second-order response of massless Dirac fermions has been extensively studied, however a general approach correct over the full Brillouin zone is lacking so far. To complete this gap, in the current paper we develop a general quantum-mechanical theory of the in-plane second-order nonlinear response beyond the Dirac cone approximation and applicable to the full Brillouin zone of the hexagonal tight-binding nanostructures. We present explicit calculation of the nonlinear susceptibility tensor of 2D hexagonal nanostructures applicable to arbitrary three-wave mixing processes,

I. INTRODUCTION

In the last decade, graphene^{1,2} and its analogs silicene,³⁻⁵ germanene,^{6,7} and stanene⁸ have attracted enormous interest due to their unique electronic and optical properties. These 2D nanostructures consist of honeycomb lattices of atoms with sublattices made of A and B sites. Hence, in their original structure free-standing honeycomb lattices are centrosymmetric, and even-order nonlinear effects at such nanostructures–light/wave interaction vanish within the dipole approximation. The latter is fully justified for the perpendicular incidence of a pump wave to the nanostructure plane. The symmetry-allowed odd-order nonlinear optical effects are very strong in graphene-like nanostructures. For graphene, this is confirmed by the experimental⁹⁻¹¹ and theoretical¹²⁻¹⁹ investigations of the third harmonic generation process. These nanomaterials can also serve as an active medium for the extreme nonlinear optical effects, such as high harmonics generation²⁰⁻³⁰.

For even-order nonlinear optical response, one should break the inversion symmetry in the mentioned nanostructures. In few-layer graphene, the inversion symmetry can be broken due to interaction between the layers which results in second harmonic generation^{31,32}. The inversion symmetry is also broken at the oblique or in-plane propagation of driving electromagnetic waves. In this case, one should take into account the spatial dispersion which results in a non-zero in-plane second-order susceptibility $\chi^{(2)}$. The second harmonic generation caused by only intraband transitions in a free-carrier model has been investigated in Refs.³³⁻³⁵. The difference-frequency generation and parametric frequency down-conversion with the emphasis on the nonlinear generation of surface plasmons have been considered in Refs.^{36,37}. The experiment³⁸ reported difference-frequency generation of surface plasmons in graphene. Electron-electron interaction corrections to Feynman diagrams describing second- and third-order non-linear-response functions have been

investigated in Ref.³⁹. Valley polarization-induced second harmonic generation^{40,41} is also reported.

In Refs.^{42,43} the full quantum-mechanical theory of the in-plane second-order nonlinear response beyond the electric dipole approximation has been developed for graphene-like nanostructures considering the low-energy dynamics in the K_+ and K_- valleys. In the recent experiment⁴⁴ the main theoretical predictions^{42,43} have been confirmed. In particular, Fermi-edge resonances at the second harmonic generation in graphene were reported, and the calculated magnitude of the effective second-order nonlinear susceptibility^{42,43} was also close to the experimental values. In general, the Dirac cone approximation is valid for photon energies much smaller than nearest-neighbor hopping transfer energy $\hbar\omega \ll \gamma_0$. In practice, the Dirac cone approximation for nonlinear optical response is valid up to energies $\gamma_0/2$. For graphene ($\gamma_0 \simeq 2.8$ eV), this involves the range of frequencies from THz to the near-infrared. For silicene and germanene $\gamma_0 \simeq 1$ eV and the Dirac cone approximation is violated for mid-infrared frequencies. Hence, at visible and deep UV frequencies of driving waves for graphene and even more for silicene, germanene, and stanene one should have microscopic theory describing nonlinear interaction beyond the Dirac cone approximation and applicable to the full Brillouin zone of the hexagonal nanostructure with tight-binding electronic states. Note that spatial dispersion induced second-order nonlinear response is nonzero for doped system and at sufficiently high doping > 0.2 eV one can omit spin-orbit coupling in silicene, germanene, and stanene considering those as gapless hexagonal nanostructures with corresponding lattice spacing a and hopping transfer energy γ_0 .

In the present work, we develop the full quantum-mechanical theory of the in-plane second-order nonlinear response beyond the Dirac cone approximation and applicable to the full Brillouin zone of a hexagonal tight-binding nanostructure. The resulting nonlinear suscepti-

bility tensor satisfies all symmetry and permutation properties and can be applied for the arbitrary wave mixing.

The paper is organized as follows. In Sec. II the Hamiltonian within the tight-binding approximation and the solution of the master equation for the density matrix are presented. In Sec. III, we calculate the second-order susceptibility tensor taking into account the spatial dispersion. Then we examine the susceptibility tensors for second-order harmonic and difference/sum-frequency generation processes. In particular, we consider the plasmon generation at the down-conversion. Finally, conclusions are given in Sec. IV.

II. THE TIGHT-BINDING HAMILTONIAN AND PERTURBATIVE SOLUTION OF THE MASTER EQUATION FOR THE DENSITY MATRIX

Let a monolayer nanostructure consisting of a honeycomb lattice (see Fig. 1) interacts with multicolor electromagnetic radiation. We consider the interaction with obliquely incident waves. A sketch of the interaction geometry is shown in Fig. 1(c). In the z -direction, we have a strong binding of the electrons. Hence, we will neglect the in-plane component of the magnetic field or out of the plane electrical field component. The light-matter interaction will be described in the velocity gauge.

The hexagonal lattice Fig. 1(a) is spanned by the basis vectors:

$$\mathbf{a}_1 = \left(\frac{\sqrt{3}a}{2}, \frac{a}{2} \right), \quad \mathbf{a}_2 = \left(\frac{\sqrt{3}a}{2}, -\frac{a}{2} \right), \quad (1)$$

with the lattice spacing a . The vectors which connect nearest neighbor atoms are:

$$\begin{aligned} \boldsymbol{\delta}_1 &= \left(\frac{a}{\sqrt{3}}, 0 \right), \quad \boldsymbol{\delta}_2 = \left(-\frac{a}{2\sqrt{3}}, \frac{a}{2} \right), \\ \boldsymbol{\delta}_3 &= \left(-\frac{a}{2\sqrt{3}}, -\frac{a}{2} \right). \end{aligned} \quad (2)$$

In reciprocal space, one can choose the hexagonal or rhombic Brillouin zone. For integration, it is convenient to choose the rhombic Brillouin zone. Fig. 1(b) formed by two vectors:

$$\mathbf{b}_1 = \left(-\frac{2\pi}{a\sqrt{3}}, \frac{2\pi}{a} \right), \quad \mathbf{b}_2 = \left(\frac{2\pi}{a\sqrt{3}}, \frac{2\pi}{a} \right). \quad (3)$$

with the reciprocal lattice spacing - $k_b = 4\pi/\sqrt{3}a$. The important crystallographic points which are crucial for electronic properties of nanostructure are also shown. High-energy excitations are situated in the vicinity of the Γ point. Low-energy excitations are centered around the two points K_+ and K_- represented by the vectors

$$\mathbf{K}_+ = \frac{k_b}{\sqrt{3}} \hat{\mathbf{y}}, \quad \mathbf{K}_- = \frac{2k_b}{\sqrt{3}} \hat{\mathbf{y}}. \quad (4)$$

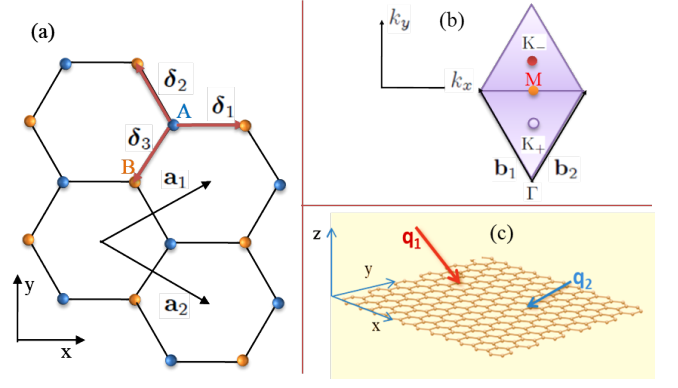


FIG. 1: (a) Hexagonal lattice in real space with two sublattices, A and B.. The vectors $\boldsymbol{\delta}_1$, $\boldsymbol{\delta}_2$, and $\boldsymbol{\delta}_3$ connect nearest neighbor atoms. The vectors $\mathbf{a}_1 = \boldsymbol{\delta}_1 - \boldsymbol{\delta}_3$ and $\mathbf{a}_2 = \boldsymbol{\delta}_1 - \boldsymbol{\delta}_2$ are the basis vectors. (b) The rhombical first Brillouin zone of reciprocal lattice with basis vectors \mathbf{b}_1 and \mathbf{b}_2 . (c) A sketch of the interaction geometry with obliquely incident waves.

Finally, it is shown M point ($\mathbf{M} = \sqrt{3}k_b \hat{\mathbf{y}}/2$).

The tight-binding Hamiltonian in the first nearest-neighbor approximation can be written as

$$\hat{H}_0 = -\gamma_0 \sum_{\langle i,j \rangle \alpha} c_{i\alpha}^\dagger c_{j\alpha}, \quad (5)$$

where $c_{i\alpha}^\dagger$ creates an electron with spin polarization α at site i , and $\langle i,j \rangle$ runs over all the first nearest-neighbor hopping sites with the transfer energy γ_0 . By performing Fourier transformations and choosing the basis $\{|A\rangle, |B\rangle\} \otimes \{|\uparrow\rangle, |\downarrow\rangle\}$, from Eq. (5) one can obtain the Hamiltonian

$$\hat{H}_0(\mathbf{k}) = \begin{bmatrix} 0 & -\gamma_0 f(\mathbf{k}) \\ -\gamma_0 f^*(\mathbf{k}) & 0 \end{bmatrix}, \quad (6)$$

where

$$f(\mathbf{k}) = \sum_{i=1}^3 \exp(i\mathbf{k} \cdot \boldsymbol{\delta}_i) = e^{i\frac{ak_x}{\sqrt{3}}} + 2e^{-i\frac{ak_x}{2\sqrt{3}}} \cos\left(\frac{ak_y}{2}\right). \quad (7)$$

Note that near the two Dirac points $\gamma_0 f(\mathbf{k}) = \hbar v_F (ik_x \mp k_y)$, where $v_F = \sqrt{3}a\gamma_0/2\hbar$ is the Fermi velocity. The spin $s_z = \pm 1$ is a good quantum number. For the issue considered, there are no spin-flip transitions and the spin index s_z can be considered as a parameter.

In the presence of radiation field with the vector potential \mathbf{A} the Hamiltonian is obtained by Peierls substitution, i.e., $\mathbf{k} \rightarrow \mathbf{k} + e\mathbf{A}/(\hbar c)$, where \hbar is the Planck's constant, e is the elementary charge, c is the light speed in vacuum. Then, the interaction Hamiltonian \hat{H}_{int} is obtained by the first-order term of \mathbf{A} from $H_0(\mathbf{k} + e\mathbf{A}/(\hbar c)) - H_0(\mathbf{k})$. Using the velocity operator $\hat{\mathbf{v}} = [\hat{\mathbf{r}}, \hat{H}_0]/i\hbar$, the interaction Hamiltonian becomes:

$$\hat{H}_{\text{int}} = \frac{e}{\hbar c} \mathbf{A} \cdot \begin{bmatrix} 0 & -\gamma_0 \nabla_{\mathbf{k}} f(\mathbf{k}) \\ -\gamma_0 \nabla_{\mathbf{k}} f^*(\mathbf{k}) & 0 \end{bmatrix}. \quad (8)$$

Note that within this tight-binding model there is no contribution arising from the z component of the vector potential. The latter describes the in plane magnetic field or out of the plane electrical field component. Taking into account Eq. (7) the velocity operator can be represented as

$$\hat{v}(\mathbf{k}) = v_F \begin{bmatrix} 0 & \mathbf{\Lambda}(\mathbf{k}) \\ \mathbf{\Lambda}^*(\mathbf{k}) & 0 \end{bmatrix}, \quad (9)$$

where

$$\Lambda_x = -\frac{2}{3}i \left(e^{i\frac{ak_x}{\sqrt{3}}} - e^{-i\frac{ak_x}{2\sqrt{3}}} \cos\left(\frac{ak_y}{2}\right) \right), \quad (10)$$

$$\Lambda_y = \frac{2}{\sqrt{3}} e^{-i\frac{ak_x}{2\sqrt{3}}} \sin\left(\frac{ak_y}{2}\right). \quad (11)$$

The vector potential is assumed to be

$$\mathbf{A}(\mathbf{r}, t) = \sum_{\delta, s=\pm} \mathbf{A}(s\omega_\delta) e^{is(\mathbf{q}_\delta \cdot \mathbf{r} - \omega_\delta t)}; \quad \mathbf{A}(-\omega_\delta) = \mathbf{A}^*(\omega_\delta), \quad (12)$$

where summation is over involved frequencies. The interaction Hamiltonian can be written as

$$\hat{H}_{\text{int}} = \frac{e}{c} \sum_{s, \delta} \hat{v}_\eta A_\eta(s\omega_\delta) e^{is(\mathbf{q}_\delta \cdot \mathbf{r} - \omega_\delta t)}. \quad (13)$$

Summation over the repeated greek indices is implied. Here \mathbf{q}_δ is the in plane wave vector.

The eigenstates of the Hamiltonian (6) with the combined quantum number $m = \{s_m, \mathbf{k}_m\}$ are:

$$\psi_m(\mathbf{r}) = |m\rangle e^{i\mathbf{k}_m \cdot \mathbf{r}}, \quad (14)$$

where

$$|m\rangle = \frac{1}{\sqrt{2}} \begin{bmatrix} e^{i\Theta(\mathbf{k}_m)} \\ s_m \end{bmatrix} \quad (15)$$

are spinors corresponding to energies

$$\mathcal{E}(m) = s_m \gamma_0 |f(\mathbf{k}_m)|. \quad (16)$$

The band index $s_m = \pm 1$: for conduction ($s_m = 1$) and valence ($s_m = -1$) bands, and $\Theta(\mathbf{k}_m) = \arg(-\gamma_0 f(\mathbf{k}_m))$.

In order to develop a microscopic theory of the non-linear interaction of a nanostructure with a multicolor radiation field we need to solve the master equation for the density matrix ρ_{mn} :

$$i\hbar \frac{\partial \rho_{mn}}{\partial t} = (\mathcal{E}(m) - \mathcal{E}(n)) \rho_{mn}$$

$$+ \sum_l \left[\langle m | \hat{H}_{\text{int}} | l \rangle \rho_{ln} - \rho_{ml} \langle l | \hat{H}_{\text{int}} | n \rangle \right] - i\hbar \gamma \left(\rho_{mn} - \rho_{mn}^{(0)} \right), \quad (17)$$

where $\rho_{mn}^{(0)}$ is the equilibrium density matrix to which the system relaxes at a rate γ . We construct $\rho_{mn}^{(0)}$ from the filling of electron states according to the Fermi-Dirac distribution:

$$\rho_{mn}^{(0)} = n_F(m) \delta_{mn},$$

where

$$n_F(m) \equiv n_F(s_m, \mathbf{k}_m) = \frac{1}{1 + \exp\left(\frac{s_m \gamma_0 |f(\mathbf{k}_m)| - \varepsilon_F}{T}\right)}. \quad (18)$$

Here ε_F is the Fermi energy and T is the temperature in energy units. Note that this relaxation approximation provides an accurate description for optical field components oscillating at frequencies $\omega \gg \gamma$.

We will solve Eq. (17) in the scope of perturbation theory:

$$\rho_{mn}(t) = \rho_{mn}^{(0)} + \rho_{mn}^{(1)}(t) + \rho_{mn}^{(2)}(t) + \dots \quad (19)$$

From Eq. (17) we have the following equations for $\rho_{mn}^{(1)}(t) \sim A$, and $\rho_{mn}^{(2)}(t) \sim A^2$:

$$i\hbar \frac{\partial \rho_{mn}^{(1)}(t)}{\partial t} = (\mathcal{E}(m) - \mathcal{E}(n) - i\hbar\gamma) \rho_{mn}^{(1)}(t)$$

$$+ \sum_l \left[\langle m | \hat{H}_{\text{int}} | l \rangle \rho_{ln}^{(0)} - \rho_{ml}^{(0)} \langle l | \hat{H}_{\text{int}} | n \rangle \right], \quad (20)$$

$$i\hbar \frac{\partial \rho_{mn}^{(2)}(t)}{\partial t} = (\mathcal{E}(m) - \mathcal{E}(n) - i\hbar\gamma) \rho_{mn}^{(2)}(t)$$

$$+ \sum_l \left[\langle m | \hat{H}_{\text{int}} | l \rangle \rho_{ln}^{(1)}(t) - \rho_{ml}^{(1)}(t) \langle l | \hat{H}_{\text{int}} | n \rangle \right]. \quad (21)$$

The solutions to Eqs. (20) and (21) are

$$\rho_{mn}^{(1)} = \frac{e}{c} \sum_{s,\delta} \frac{A_\eta(s\omega_\delta) \exp(-is\omega_\delta t) \langle m | \hat{v}_\eta e^{is\mathbf{q}_\delta \mathbf{r}} | n \rangle}{\mathcal{E}(m) - \mathcal{E}(n) - s\hbar\omega_\delta - i\hbar\gamma} (n_F(m) - n_F(n)), \quad (22)$$

$$\begin{aligned} \rho_{mn}^{(2)} &= \frac{e^2}{c^2} \sum_l \sum_{s,\delta} \sum_{s_1,\delta_1} \frac{A_\beta(s_1\omega_{\delta_1}) A_\eta(s\omega_\delta) \exp(-i(s_1\omega_{\delta_1} + s\omega_\delta)t)}{\mathcal{E}(m) - \mathcal{E}(n) - \hbar(s_1\omega_{\delta_1} + s\omega_\delta) - i\hbar\gamma} \\ &\times \left[\frac{\langle m | \hat{v}_\beta e^{is_1\mathbf{q}_{\delta_1} \mathbf{r}} | l \rangle \langle l | \hat{v}_\eta e^{is\mathbf{q}_\delta \mathbf{r}} | n \rangle}{\mathcal{E}(m) - \mathcal{E}(l) - s_1\hbar\omega_{\delta_1} - i\hbar\gamma} (n_F(m) - n_F(l)) - \frac{\langle m | \hat{v}_\eta e^{is\mathbf{q}_\delta \mathbf{r}} | l \rangle \langle l | \hat{v}_\beta e^{is_1\mathbf{q}_{\delta_1} \mathbf{r}} | n \rangle}{\mathcal{E}(l) - \mathcal{E}(n) - s_1\hbar\omega_{\delta_1} - i\hbar\gamma} (n_F(l) - n_F(n)) \right]. \quad (23) \end{aligned}$$

With the help of solution (23) one can calculate physical observables to investigate second order nonlinear response of 2D nanostructures.

III. SECOND ORDER NONLINEAR RESPONSE OF 2D HEXAGONAL NANOSTRUCTURE

With the help of solutions (22) and (23) of the quantum master equation (17), obtained in the previous section, one can investigate the linear and second-order nonlinear electromagnetic response of hexagonal nanostructure. The linear response beyond the Dirac cone approximation is well investigated² and we will concentrate on the second-order nonlinear electromagnetic response. Along with the graphene we will present the results for silicene. Germanene and stanene have parameters close to silicene and the results for these materials will be almost identical. We will consider the spectral range when Brillouin zone of a hexagonal tight-binding nanostructure is excited out of Dirac two cones. First, we calculate the second-order conductivity tensor. For this we will take into account the relations

$$j_\alpha(\omega, \mathbf{q}) = -g_s e \sum_{mn} \langle n | \hat{v}_\alpha e^{-i\mathbf{q} \cdot \mathbf{r}} | m \rangle \rho_{mn}^{(2)}(\omega), \quad (24)$$

and

$$\begin{aligned} j_\alpha(\omega_3, \mathbf{q}_3) &= \sigma_{\alpha\beta\eta}(\omega_3, \mathbf{q}_3; \omega_1, \mathbf{q}_1, \omega_2, \mathbf{q}_2) E_\beta(\omega_1) E_\eta(\omega_2) \\ &= \sigma_{\alpha\beta\eta}(\omega_3, \mathbf{q}_3; \omega_1, \mathbf{q}_1, \omega_2, \mathbf{q}_2) \frac{\omega_1 \omega_2}{c^2} A_\beta(\omega_1) A_\eta(\omega_2), \quad (25) \end{aligned}$$

where $g_s = 2$ is the spin degeneracy factor, $E_\alpha(\omega_1)$ is the electrical field strength Fourier amplitude. From Eqs. (23), (24) and (25) for the second order conductivity tensor we obtain

$$\begin{aligned} \sigma_{\alpha\beta\eta}^{(2)}(\omega_3, \mathbf{q}_3; \omega_1, \mathbf{q}_1, \omega_2, \mathbf{q}_2) &= -\frac{2e^3}{\omega_1 \omega_2} \sum_{mnl} \frac{\langle n | \hat{v}_\alpha e^{-i\mathbf{q}_3 \cdot \mathbf{r}} | m \rangle}{\mathcal{E}(m) - \mathcal{E}(n) - \hbar(\omega_1 + \omega_2) - i\hbar\gamma} \\ &\times \left[\frac{\langle m | \hat{v}_\beta e^{i\mathbf{q}_1 \mathbf{r}} | l \rangle \langle l | \hat{v}_\eta e^{i\mathbf{q}_2 \mathbf{r}} | n \rangle}{\mathcal{E}(m) - \mathcal{E}(l) - \hbar\omega_1 - i\hbar\gamma} (n_F(m) - n_F(l)) - \frac{\langle m | \hat{v}_\eta e^{i\mathbf{q}_2 \mathbf{r}} | l \rangle \langle l | \hat{v}_\beta e^{i\mathbf{q}_1 \mathbf{r}} | n \rangle}{\mathcal{E}(l) - \mathcal{E}(n) - \hbar\omega_1 - i\hbar\gamma} (n_F(l) - n_F(n)) \right. \\ &\left. + \frac{\langle m | \hat{v}_\eta e^{i\mathbf{q}_2 \mathbf{r}} | l \rangle \langle l | \hat{v}_\beta e^{i\mathbf{q}_1 \mathbf{r}} | n \rangle}{\mathcal{E}(m) - \mathcal{E}(l) - \hbar\omega_2 - i\hbar\gamma} (n_F(m) - n_F(l)) - \frac{\langle m | \hat{v}_\beta e^{i\mathbf{q}_1 \mathbf{r}} | l \rangle \langle l | \hat{v}_\eta e^{i\mathbf{q}_2 \mathbf{r}} | n \rangle}{\mathcal{E}(l) - \mathcal{E}(n) - \hbar\omega_2 - i\hbar\gamma} (n_F(l) - n_F(n)) \right]. \quad (26) \end{aligned}$$

The transition matrix elements for velocity operator (9) can be calculated with the help of Eqs. (10), (11), (14), and (15). As a result we obtain

$$\langle n | \hat{v}_\alpha e^{i\mathbf{q} \cdot \mathbf{r}} | m \rangle = v_F \Lambda_\alpha(s_m, \mathbf{k}_m, s_n, \mathbf{k}_n) (2\pi)^2 \delta(\mathbf{k}_m + \mathbf{q} - \mathbf{k}_n), \quad (27)$$

where

$$\Lambda(s_m, \mathbf{k}_m, s_n, \mathbf{k}_n) = \frac{1}{2} \left[s_m \Lambda(\mathbf{k}_m) e^{-i\Theta(\mathbf{k}_n)} + s_n \Lambda^*(\mathbf{k}_m) e^{i\Theta(\mathbf{k}_m)} \right].$$

The Dirac delta function in Eq. (27) expresses conservation law for momentum. Taking into account these relations, the second order conductivity tensor (26) can be written as

$$\sigma_{\alpha\beta\eta}^{(2)}(\omega_3, \mathbf{q}_3; \omega_1, \mathbf{q}_1, \omega_2, \mathbf{q}_2) = F_{\alpha\beta\eta}(\omega_1, \mathbf{q}_1, \omega_2, \mathbf{q}_2) + F_{\alpha\eta\beta}(\omega_2, \mathbf{q}_2, \omega_1, \mathbf{q}_1), \quad (28)$$

where

$$F_{\alpha\beta\eta}(\omega_1, \mathbf{q}_1, \omega_2, \mathbf{q}_2) = -\frac{2e^3 v_F^3}{\omega_1 \omega_2} \frac{1}{(2\pi)^2} \sum_{s_m, s_n, s_l} \int_{BZ} d\mathbf{k} \frac{\Lambda_\alpha(s_m, \mathbf{k} + \mathbf{q}_1, s_n, \mathbf{k} - \mathbf{q}_2) \Lambda_\beta(s_l, \mathbf{k}, s_m, \mathbf{k} + \mathbf{q}_1) \Lambda_\eta(s_n, \mathbf{k} - \mathbf{q}_2, s_l, \mathbf{k})}{s_m \gamma_0 |f(\mathbf{k} + \mathbf{q}_1)| - s_n \gamma_0 |f(\mathbf{k} - \mathbf{q}_2)| - \hbar(\omega_1 + \omega_2) - i\hbar\gamma} \\ \times \left[\frac{n_F(s_m, \mathbf{k} + \mathbf{q}_1) - n_F(s_l, \mathbf{k})}{s_m \gamma_0 |f(\mathbf{k} + \mathbf{q}_1)| - s_l \gamma_0 |f(\mathbf{k})| - \hbar\omega_1 - i\hbar\gamma} - \frac{n_F(s_l, \mathbf{k}) - n_F(s_n, \mathbf{k} - \mathbf{q}_2)}{s_l \gamma_0 |f(\mathbf{k})| - s_n \gamma_0 |f(\mathbf{k} - \mathbf{q}_2)| - \hbar\omega_2 - i\hbar\gamma} \right]. \quad (29)$$

As is seen from Eqs. (28) the conductivity tensor is symmetric in its components and arguments:

$$\sigma_{\alpha\eta\beta}^{(2)}(\omega_3, \mathbf{q}_3; \omega_2, \mathbf{q}_2, \omega_1, \mathbf{q}_1) = \sigma_{\alpha\beta\eta}^{(2)}(\omega_3, \mathbf{q}_3; \omega_1, \mathbf{q}_1, \omega_2, \mathbf{q}_2).$$

Let us consider the second-order conductivity tensor given by Eq. (28). Following convention⁴⁵, we have written $\sigma_{\alpha\beta\eta}(\omega_3, \mathbf{q}_3; \omega_1, \mathbf{q}_1, \omega_2, \mathbf{q}_2)$ as a function of three frequencies and wave vectors. The first two arguments are associated with the time-space dependence of the resulting field $\exp(i\mathbf{q}_3\mathbf{r} - i\omega_3 t)$ and we have energy and momentum conservation: $\omega_3 = \omega_1 + \omega_2$ and $\mathbf{q}_3 = \mathbf{q}_1 + \mathbf{q}_2$ at the three wave mixing. Thus, we have mutual interaction of three waves and for a complete description of the interaction of these waves we need to determine the tensors $\sigma_{\alpha\beta\eta}(\omega_3, \mathbf{q}_3; \omega_1, \mathbf{q}_1, \omega_2, \mathbf{q}_2)$, $\sigma_{\alpha\beta\eta}(\omega_1, \mathbf{q}_1; \omega_3, \mathbf{q}_3, -\omega_2, -\mathbf{q}_2)$, and $\sigma_{\alpha\beta\eta}(\omega_2, \mathbf{q}_2; \omega_3, \mathbf{q}_3 - \omega_1, -\mathbf{q}_1)$, wherein we have two independent frequencies and wavevectors. In particular $\sigma_{\alpha\beta\eta}(\omega_3, \mathbf{q}_3; \omega_1, \mathbf{q}_1, \omega_2, \mathbf{q}_2)$ is responsible for the sum-frequency generation. At $\omega_1 = \omega_2 \equiv \omega$ we have the second harmonic generation process. The tensor $\sigma_{\alpha\beta\eta}(\omega_1, \mathbf{q}_1; \omega_3, \mathbf{q}_3, -\omega_2, -\mathbf{q}_2)$ is responsible for the difference-frequency generation. In this case ω_3 is known as the pump frequency, ω_2 the signal frequency, and ω_1 the idler frequency. In the next, we will consider these processes separately.

With the help of conductivity tensor in CGS units, one can calculate also susceptibility tensor in SI units by the formula

$$\chi_{\alpha\beta\eta}(\omega_3, \mathbf{q}_3; \omega_1, \mathbf{q}_1, \omega_2, \mathbf{q}_2) \\ = \frac{4\pi i}{\omega_3} \sigma_{\alpha\beta\eta}(\omega_3, \mathbf{q}_3; \omega_1, \mathbf{q}_1, \omega_2, \mathbf{q}_2). \quad (30)$$

For easier comparison of the nonlinear response of the considered nanostructure with known materials hereafter we will calculate susceptibility tensor in SI units. For the final result Eq. (29) should be integrated over the Brillouin zone for a given geometry of the incident fields, Fermi energy, and temperature. It contains intraband contributions (two terms), as well as all types of mixed

interband and intraband contributions (six terms). For normal incidence ($\mathbf{q}_1 = \mathbf{q}_2 = 0$) $\chi_{\alpha\beta\eta} = 0$ as expected from inversion symmetry of considered nanostructure. For hexagonal nanostructure (Fig. 1(c)), we have two directions of interest for in-plane wave vectors: along the zigzag direction or armchair one. As expected from the symmetry, the results are identical. For concreteness, we will direct all in-plane photon wave vectors along the x -axis (3D wave vectors in the ZX plane). In this case nonzero components are $\chi_{xxx}, \chi_{xyy}, \chi_{yxy}, \chi_{yyx}$. Here χ_{xxx}, χ_{xyy} describe the generation of the p-polarized wave with p-polarized and s-polarized waves, correspondingly. Then χ_{yxy} and χ_{yyx} describe the generation of the s-polarized waves with mixed waves. Note that $\chi_{yxx} = 0$, since p-polarized input waves can not generate s-polarized output wave.

It is clear that due to the electron-hole symmetry the absolute value of the second-order susceptibility tensor is the same for $\pm\varepsilon_F$. Thus, we will consider only the electron-doped system $\varepsilon_F > 0$. From Eq. (29) it is seen that the second-order susceptibility will have peaks when involved frequencies are nearly resonant with the $2\varepsilon_F/\hbar$ so-called Fermi-edge resonances. At that, one can realize an efficient second harmonic generation process or optical parametric amplifier pumped close to the $2\varepsilon_F/\hbar$. In this regard note that obtained formulas are not valid for small frequencies $\omega \lesssim \gamma$, and $\chi_{\alpha\beta\eta}$ diverges at $\omega \rightarrow 0$. Besides, since we adopted an independent quasiparticle picture, one should be also careful at applying the obtained results to far off-resonant pump waves. At the excitations of nanostructure with the waves $\hbar\omega \gg \varepsilon_F$ one triggers photoexcitation cascade and, as a result, the multiple hot carrier generation takes place in the nanostructure⁴⁶. Meanwhile, near the Fermi level, these processes are suppressed and we have the dominant contribution of pure optical transitions, thus Eq. (30) can accurately describe second-order nonlinear optical response for optical field components oscillating at frequencies $\omega \gg \gamma$.

A. Sum-frequency generation process in 2D hexagonal nanostructure

Let us first consider the susceptibility of 2D hexagonal nanostructure $\chi_{\alpha\beta\eta}(2\omega, 2q_x; \omega, q_x, \omega, q_x)$ responsible for the second harmonic generation. Note that the intensity of the second harmonic wave depends on the absolute value $|\chi_{\alpha\beta\eta}|$ ⁴⁵. In Figs. 2 and 3 we plot nonzero components of the second-order susceptibility tensor for silicene ($a = 3.86 \times 10^{-8}$ cm, $\gamma_0 = 1.087$ eV) and graphene ($a = 2.46 \times 10^{-8}$ cm, $\gamma_0 = 2.8$ eV) for various Fermi energies as a function of the fundamental frequency. The pump waves are incident at $\pi/4$ ($q_x = \omega/(c\sqrt{2})$). In both figures, we observe comparable values for both nanostructures with peaks near the Fermi energy (second harmonic $\omega_3 \simeq 2\varepsilon_F/\hbar$) and double Fermi energy ($\omega_1 = \omega_2 \simeq 2\varepsilon_F/\hbar$). These are Fermi-edge resonances predicted in Refs.^{42,43}. In Fig. 2, at $\varepsilon_F = 725$ meV for graphene the Dirac cone approximation is valid and near the Fermi energy isoenergy contours are isotropic, and as a consequence, the maximal values of all components are equal. For silicene $\varepsilon_F \sim \gamma_0$, the isoenergy contours are nonisotropic and maximal values are different. For larger Fermi energy this anisotropy is reflected also for graphene in Fig. 3. In Fig 4, we plot results calculated with the parameters taken from the experiment⁴⁴ by Zhang et al. For comparison with the experiment in Fig. 4, we plotted the equivalent susceptibility for a bulk, which is calculated dividing $\chi_{\alpha\beta\eta}$ by the effective thickness of the monolayer. For both nanostructures we assume $d_{\text{eff}} \approx 0.3$ nm. The results for graphene are in good agreement with experiment⁴⁴ by Zhang et al. As is seen, for the fixed frequency the susceptibility tensor grows rapidly as ε_F approaches the Fermi-edge resonances at one-photon ($2\varepsilon_F = \hbar\omega$) and two-photon ($\varepsilon_F = \hbar\omega$) energies. Note that in Refs.^{42,43} Fermi-edge resonances is attributed to the resonant transitions in the linearly dispersed band structure of graphene. As we see from Figs. 2(a), 3(a), and 4(a), for silicene the Dirac cone approximation is not valid but we have similar Fermi-edge resonances.

In Fig. 5, the maximum values of the second-order susceptibility tensor components for the process of second harmonic generation as a function of the Fermi energy for silicene and graphene are shown. As is seen, with the increase of Fermi energy and consequently resonant frequency the maximum value of susceptibility tensor is reduced. For graphene one can interpolate the dependence $\chi_{\alpha\beta\eta} \sim 1/\varepsilon_F^2$, which is also clear from the analytical result⁴². For silicene, the interpolation $\chi_{\alpha\beta\eta} \sim 1/\varepsilon_F^2$ is valid up to energies $\varepsilon_F \simeq 0.7\gamma_0$. From the inset of Fig. 5(a) we see that for silicene near 1 eV we have a local maximum. The latter takes place when one of the driving waves is in one photon resonance with the van Hove singularity at the M point of Brillouin zone. Near the M point, the energy dispersion curves of considered nanostructures flatten, and thus the density of states is high because of the van Hove singularity at

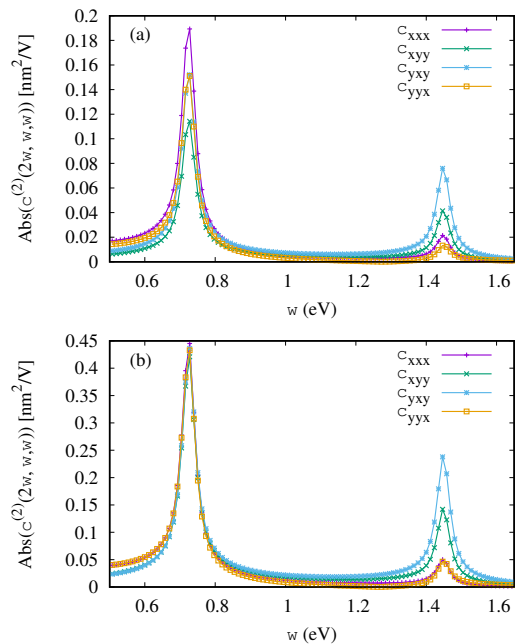


FIG. 2: Nonzero components of the second order susceptibility tensor for the process of second-harmonic generation as a function of the fundamental frequency for silicene (a) and for graphene (b). The pump waves are incident at $\pi/4$. The Fermi energy is $\varepsilon_F = 725$ meV. The temperature is $T = 3$ meV. The relaxation rate is taken to be $\hbar\gamma = 5$ meV.

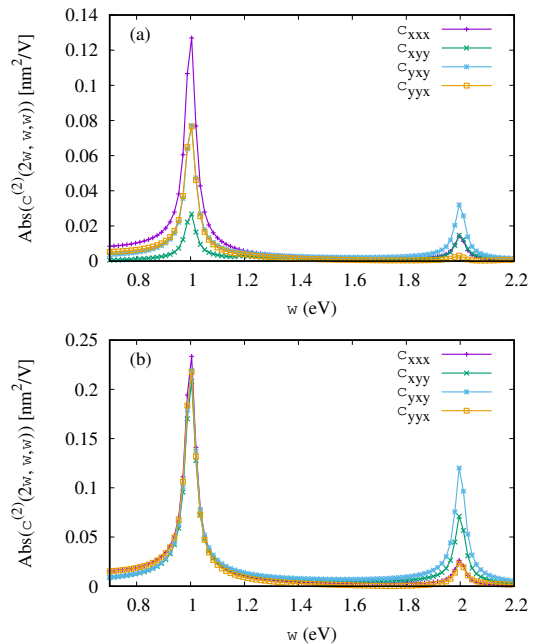


FIG. 3: The same as in Fig. 2, but for the Fermi energy $\varepsilon_F = 1$ eV.

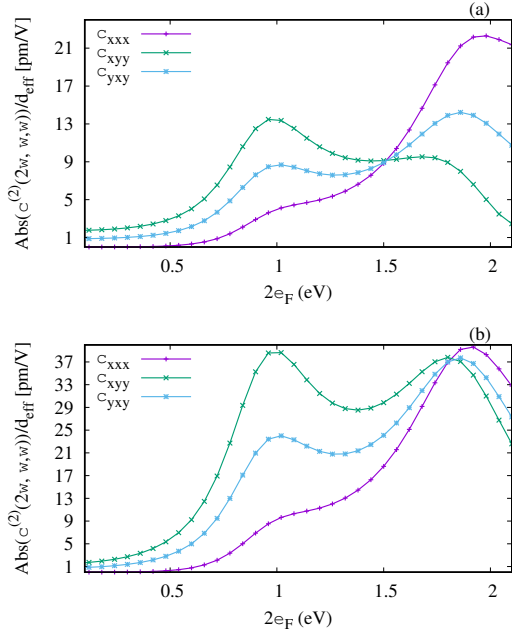


FIG. 4: The second order susceptibility tensor components for the process of second-harmonic generation as a function of the Fermi energy for silicene (a) and for graphene (b). The frequency is $\hbar\omega = 0.95$ eV. The pump waves are incident at $\pi/4$. The temperature is $T = 26$ meV. The relaxation rate is taken to be $\hbar\gamma = 0.2\varepsilon_F$.

the saddle point, thereby one has an enhancement of the nonlinear optical response of considered nanostructure. Note that for graphene the van Hove resonant frequency $2\gamma_0$ is in the UV domain. We have also investigated the temperature dependence of the maximum values of the second-order susceptibility tensor components for second harmonic generation process. The latter is plotted for graphene in Fig. 6 at the various Fermi energies. The same picture we have for the silicene. From Fig. 6 one can interpolate the dependence $\chi_{\alpha\beta\eta} \sim 1/T$. The latter strictly restricts the second harmonic generation process at the room temperatures. The maximum value of the calculated second-order susceptibility for the second harmonic generation at the resonances are: $|\chi_{\alpha\beta\eta}(2\omega; \omega, \omega)|_{\max} \simeq 0.1 - 0.4$ nm²/V. Thus, for the bulk we obtain $|\chi_{\alpha\beta\eta}(2\omega; \omega, \omega)|_{\max}/d_{\text{eff}} \simeq 300 - 1000$ pm/V. Compared with common materials for the second-order nonlinearity these values are very large. For the lithium niobate $\chi^{(2)} \simeq 20$ pm/V.

For the second harmonic generation, we have resonance when the output radiation is close to $2\varepsilon_F/\hbar$. In case, when one of the pump frequencies is very small compared to other: $\omega_2 \ll \omega_1$, one can realize a double resonance $\omega_1 \simeq \omega_3 \sim 2\varepsilon_F/\hbar$ with the considerable enhancement of the output nonlinear response. Thus, in Fig. 7 the absolute values of susceptibility tensor components responsible for sum-frequency generation as a function of one of the pump frequencies ω_1 for silicene and for

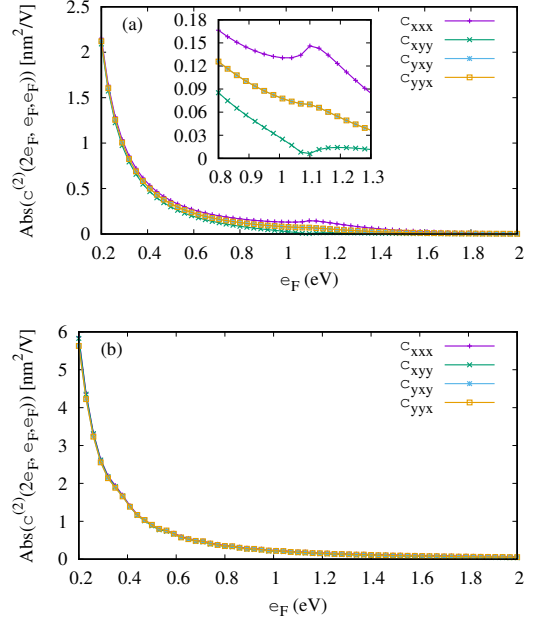


FIG. 5: The maximum values of the second order susceptibility tensor components for the process of second-harmonic generation as a function of the Fermi energy for silicene (a) and for graphene (b). The pump waves are incident at $\pi/4$. The temperature is $T = 3$ meV. The relaxation rate is taken to be $\hbar\gamma = 5$ meV.

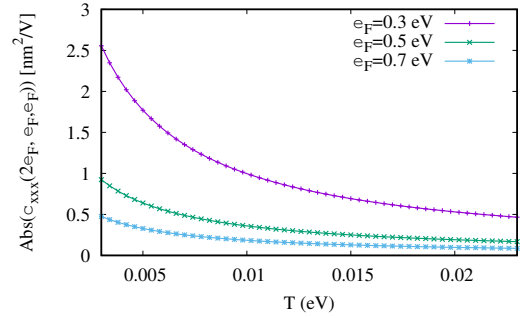


FIG. 6: The maximum values of the second order susceptibility tensor components for the process of second-harmonic generation as a function of the temperature for graphene at various Fermi energies. The pump waves are incident at $\pi/4$. The relaxation rate is taken to be $\hbar\gamma = 5$ meV.

graphene are displayed. As is seen, we have maximal enhancement when the low-frequency pump wave is p-polarized. At that, the equivalent susceptibility for bulk is $|\chi_{\alpha\beta\eta}|_{\max}/d_{\text{eff}} \simeq 1.5 \times 10^4 - 6 \times 10^4$ pm/V. Thus, at the double resonance susceptibility reaches huge values that is more pronounced for difference frequency generation process.

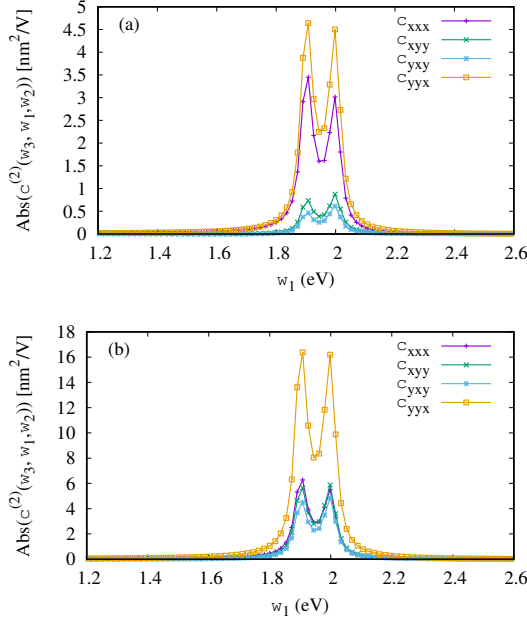


FIG. 7: The absolute values of susceptibility tensor components responsible for sum-frequency generation as a function of one of the pump frequencies ω_1 for silicene (a) and for graphene (b). The frequency ω_2 is fixed at 0.1 eV. The pump waves are incident at $\pi/4$. The Fermi energy is $\varepsilon_F = 1$ eV. The temperature is $T = 3$ meV. The relaxation rate is taken to be $\hbar\gamma = 5$ meV.

B. Difference frequency generation processes: generation of plasmons

It is also of interest the difference frequency generation processes in the considered nanostructures, since it can be used for all-optical generation of plasmons or THz radiation from visible light. For this propose we examine the susceptibility tensor $\chi_{\alpha\beta\eta}(\omega_3, \mathbf{q}_3; \omega_1, \mathbf{q}_1, -\omega_2, -\mathbf{q}_2)$. In Fig. 8 the absolute values of susceptibility tensor components responsible for difference frequency generation as a function of the pump frequency ω_1 at the fixed idler frequency $\hbar\omega_3 = 0.1\varepsilon_F$ are plotted for graphene and silicene. The maximal values of susceptibility tensors correspond cases when the output radiation is p-polarized. As is seen from this figure, even for such high frequency pump and signal waves the both nanostructures exhibit large values of $|\chi_{\alpha\beta\eta}|_{\max}/d_{\text{eff}} \simeq 1.5 \times 10^4$ pm/V. Next, we consider double resonant plasmon generation with the oblique incidence of pump and signal electromagnetic waves. For graphene, the effective spin-orbit coupling is negligibly small. However for silicene, germanene, and stanene, spin-orbit coupling opens gap ε_{soc} . For silicene $\varepsilon_{soc} \simeq 8$ meV. At $\varepsilon_F \gg \varepsilon_{soc}$ in case of graphene and silicene we can use the following dispersion relation for plasmon:

$$\hbar\omega_p(q) = \sqrt{\frac{2\alpha\varepsilon_F\hbar cq}{\varepsilon}}, \quad (31)$$

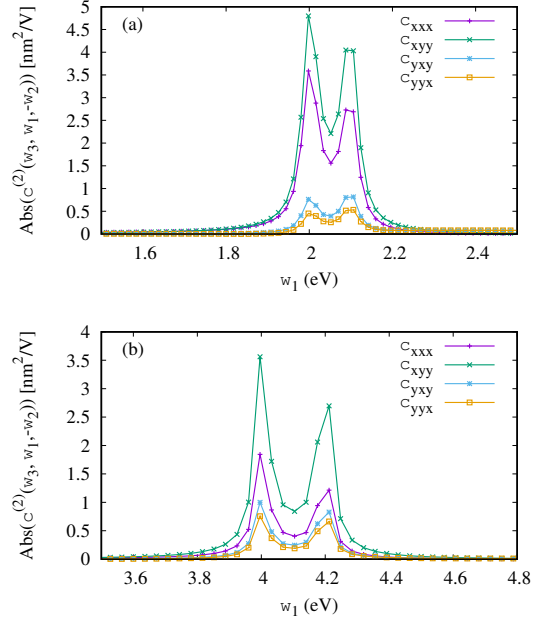


FIG. 8: The absolute values of susceptibility tensor components responsible for difference frequency generation as a function of the pump frequency ω_1 at the fixed idler frequency $\omega_3 = 0.1\varepsilon_F$. The pump and the signal waves are incident at $\pi/4$. The temperature is $T = 3$ meV. The relaxation rate is taken to be $\hbar\gamma = 5$ meV. (a) For silicene at $\varepsilon_F = 1$ eV and (b) for graphene at $\varepsilon_F = 2$ eV.

where q is the wave vector, $\alpha = 1/137$ is the fine structure constant. Here, $\varepsilon \equiv (\varepsilon_1 + \varepsilon_2)/2$, with the dielectric constants of the above ε_1 and below ε_2 surrounding media. For the plasmon generation we need to satisfy the phase-matching conditions:

$$\hbar\omega_1 - \hbar\omega_2 = \hbar\omega_p(q),$$

and

$$\mathbf{q}_1 - \mathbf{q}_2 = \mathbf{q}.$$

Assuming that pump and signal waves are incident from the vacuum ($\varepsilon_1 = 1$), the plasmon frequency is fixed: $\hbar\omega_p = 0.1\varepsilon_F$, and all in-plane photon wave vectors are directed along the x -axis with $\vartheta_2 = \pi - \vartheta_1$, for the resonant incident angle we will have

$$\cos \vartheta_1 = \frac{\varepsilon}{200\alpha} \frac{\varepsilon_F}{\hbar\omega_1 + \hbar\omega_2}.$$

We will assume a silicon dioxide substrate ($\varepsilon = 2.75$). In Fig. 9 the absolute values of susceptibility tensor components responsible for plasmon generation as a function of the pump frequency ω_1 at the fixed idler frequency $\hbar\omega_3 = \hbar\omega_p = 0.1\varepsilon_F$ for various Fermi energies are displayed. Near the resonant frequencies $\hbar\omega_1 \simeq \hbar\omega_2 \simeq 2\varepsilon_F$, the resonant incident angle is $\vartheta_1 \simeq \pi/3$. As is seen from Fig. 9, the plasmon generation is more preferable by the s-polarized waves. For both nanostructures

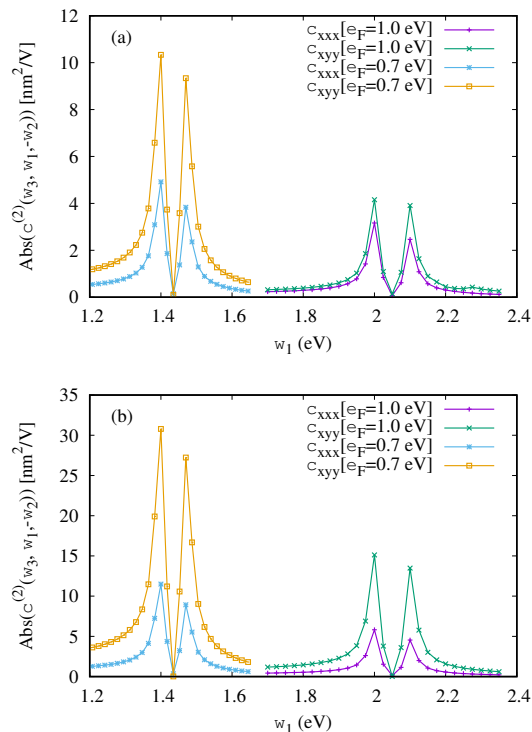


FIG. 9: The absolute values of susceptibility tensor components responsible for plasmon generation as a function of the pump frequency ω_1 at the fixed idler frequency $\omega_3 = \omega_p = 0.1\varepsilon_F$ for various Fermi energies. In plane wave vectors of the pump and the signal waves are opposite. The temperature is $T = 2$ meV. The relaxation rate is taken to be $\hbar\gamma = 5$ meV. (a) For silicene and (b) for graphene.

the maximum value of the calculated second-order susceptibility for the plasmon generation processes due to the double resonance can reach huge values as high as $|\chi_{\alpha\beta\eta}|_{\max} \simeq 30 \text{ nm}^2/\text{V}$.

We have also investigated the temperature and the relaxation rate dependence on the maximum values of the second-order susceptibility tensor components for the plasmon generation process. Figure 10 represents the density plot of the maximum values of susceptibility tensor component χ_{xxx} responsible for plasmon generation as a function of the temperature and relaxation rate. The pump frequency $\hbar\omega_1 = 2\varepsilon_F$ and the signal frequency is $\hbar\omega_2 = 1.9\varepsilon_F$. From Fig. 10 one can interpolate the dependence $\chi_{\alpha\beta\eta} \sim 1/(T^{6/5}\gamma^{1/2})$.

Let us make some estimation and compare our results with the other ones. The maximum value of the calculated second-order susceptibility for the plasmon generation processes corresponds to a bulk of $\sim 10^5$ pm/V. In this case the off-resonance susceptibility $|\chi_{\alpha\beta\eta}|_{\text{off}} \simeq 3 \text{ nm}^2/\text{V}$, which corresponds to a bulk of $\sim 10^4$ pm/V. Regarding the experimental results. Constant et al.³⁸ reported a bulk susceptibility 10^5 pm/V for off resonant plasmon generation with the waves of frequencies $\simeq 2$ eV and doping level $\varepsilon_F = 0.5$ eV. The reported value is

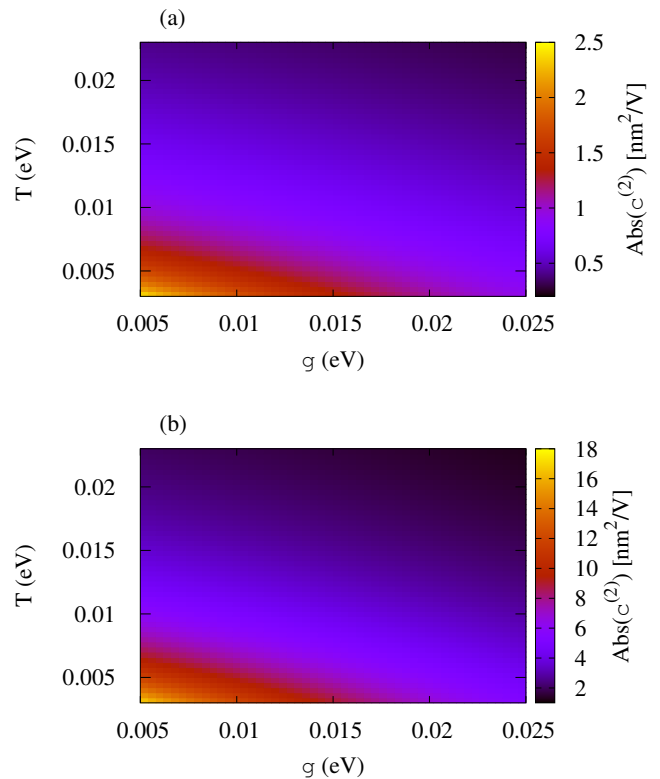


FIG. 10: The density plot of the maximum values of susceptibility tensor component χ_{xxx} responsible for plasmon generation as a function of the temperature and relaxation rate. The pump frequency $\omega_1 = 2\varepsilon_F$ and the signal frequency is $\omega_2 = 1.9\varepsilon_F$. (a) For silicene at Fermi energy 0.8 eV and (b) for graphene at Fermi energy 0.5 eV.

close to our theoretical result but for resonant susceptibility. Our off resonant susceptibility is order of magnitude smaller than the experimental one. As was mentioned above, at off-resonant generation of plasmons one should take into account the many-body effects. In particular, multiple hot carrier generation⁴⁶. In this case the independent carrier picture is not applicable.

IV. CONCLUSION

We have developed a microscopic quantum ansatz for analytical and numerical calculation of the second-order nonlinear response of hexagonal 2D nanostructures (graphene and its analogs -silicene, germanene, and stanene) beyond the Dirac cone approximation, which is applicable to the excitations in the full Brillouin zone. The second-order nonlinear optical susceptibility tensor has been calculated for monolayers of graphene and silicene. We have demonstrated that Fermi-edge resonances also take place for the high-frequency excitations beyond the linear dispersion of massless Dirac fermions. For visible and UV frequencies both nanostructures exhibit

a large second-order response. For the difference/sum-frequency generation processes, one can realize double resonance – when the pump wave frequency and the idler frequency are close to double Fermi energy– the second-order susceptibility reaches huge values. The obtained results show that along with graphene at sufficiently high doping silicene, germanene, and stanene are promising materials for optoelectronic applications. In particular, these materials are ideally suited for the all-optical plasmon generation at the double Fermi-edge resonances. We have also investigated temperature (T) and relaxation rate (γ) dependences of the second-order sus-

ceptibility tensor components for the process of plasmon generation which in the wide range show the dependence $\chi_{\alpha\beta\eta} \sim 1/(T^{6/5}\gamma^{1/2})$.

Acknowledgments

This work was supported by the RA State Committee of Science and Belarusian Republican Foundation for Fundamental Research (RB) in the frame of the joint research project SCS 18BL-020.

-
- ¹ K. S. Novoselov, A. K. Geim, S. V. Morozov, D. Jiang, Y. Zhang, S. V. Dubonos, I. V. Grigorieva, and A. A. Firsov, *Science* **306**, 666 (2004).
 - ² A. H. Castro Neto, F. Guinea, N. M. R. Peres, K. S. Novoselov, and A. K. Geim, *Rev. Mod. Phys.* **81**, 109 (2009).
 - ³ B. Lalimi, H. Oughaddou, H. Enriquez, A. Kara, S. Vizzini, B. Ealet, and B. Aufray, *Applied Physics Letters* **97**, 223109 (2010).
 - ⁴ P. Vogt, P. De Padova, C. Quaresima, J. Avila, E. Frantzeskakis, M.C. Asensio, A. Resta, B. Ealet and G. Le Lay, *Phys. Rev. Lett.* **108**, 155501 (2012).
 - ⁵ A. Fleurence, R. Friedlein, T. Ozaki, H. Kawai, Y. Wang, and Y. Yamada-Takamura, *Phys. Rev. Lett.* **108**, 245501 (2012).
 - ⁶ E. Bianco, S. Butler, S. Jiang, O. D. Restrepo, W. Windl, J. E. Goldberger, *Acs Nano* **7**, 4414 (2013).
 - ⁷ M. E. Davila, , L. Xian, S. Cahangirov, A. Rubio, and G. L. Lay, *New Journal of Physics* **16**, 095002 (2014).
 - ⁸ F.F. Zhu, W.J. Chen, Y. Xu, C.L. Gao, D.D. Guan, C.H. Liu, D. Qian, S.C. Zhang, J.F. Jia, *Nature Materials* **14**, 1020 (2015).
 - ⁹ E. Hendry, P.J. Hale, J. Moger, A.K. Savchenko, and S.A. Mikhailov, *Phys. Rev. Lett.* **105**, 097401 (2010).
 - ¹⁰ N. Kumar, J. Kumar, C. Gerstenkorn, R. Wang, H.-Y. Chiu, A.L. Smirl, and H. Zhao, *Phys. Rev. B* **87**, 121406(R) (2013).
 - ¹¹ S.-Y. Hong, J.I. Dadap, N. Petrone, P.-C. Yeh, J. Hone, and R.M. Osgood, Jr., *Phys. Rev. X* **3**, 021014 (2013).
 - ¹² S.A. Jafari, *J. Phys.: Condens. Matter* **24**, 205802 (2012).
 - ¹³ S.A. Mikhailov, *Phys. Rev. B* **90**, 241301(R) (2014).
 - ¹⁴ J.L. Cheng, N. Vermeulen, and J.E. Sipe, *New J. Phys.* **16**, 053014 (2014).
 - ¹⁵ J.L. Cheng, N. Vermeulen, and J.E. Sipe, *Phys. Rev. B* **91**, 235320 (2015).
 - ¹⁶ S.A. Mikhailov, *Phys. Rev. B* **93**, 085403 (2016).
 - ¹⁷ I. Al-Naib, M. Poschmann, and M. M. Dignam, *Phys. Rev. B* **91**, 205407 (2015).
 - ¹⁸ H. Rostami and M. Polini, *Phys. Rev. B* **93**, 161411 (2016).
 - ¹⁹ Z. Sun, D. N. Basov, and M. M. Fogler, *arXiv:1710.02297v2* (2017).
 - ²⁰ S. A. Mikhailov, K. Ziegler, *J. Phys. Condens. Matter* **20**, 384204 (2008).
 - ²¹ H. K. Avetissian, A. K. Avetissian, G. F. Mkrtchian, Kh. V. Sedrakian, *Phys. Rev. B* **85**, 115443 (2012).
 - ²² H. K. Avetissian, G. F. Mkrtchian, K. G. Batrakov, S. A. Maksimenko, A. Hoffmann, *Phys. Rev. B* **88**, 165411 (2013).
 - ²³ P. Bowlan, E. Martinez-Moreno, K. Reimann, T. Elsaesser, and M. Woerner, *Phys. Rev. B* **89**, 041408 (2014).
 - ²⁴ I. Al-Naib, J. E. Sipe, and M. M. Dignam, *Phys. Rev. B* **90**, 245423 (2014).
 - ²⁵ L. A. Chizhova, F. Libisch, and J. Burgdorfer, *Phys. Rev. B* **95**, 085436 (2017).
 - ²⁶ D. Dimitrovski, L. B. Madsen, and T. G. Pedersen, *Phys. Rev. B* **95**, 035405 (2017).
 - ²⁷ N. Yoshikawa, T. Tamaya, and K. Tanaka, *Science* **356**, 736 (2017).
 - ²⁸ H. K. Avetissian, G. F. Mkrtchian, *Phys. Rev. B* **97**, 115454 (2018).
 - ²⁹ H. K. Avetissian, G. F. Mkrtchian, *Phys. Rev. B* **99**, 085432 (2019).
 - ³⁰ H. K. Avetissian, A. K. Avetissian, B. R. Avchyan, G. F. Mkrtchian, *Phys. Rev. B* **100**, 035434 (2019).
 - ³¹ J. J. Dean and H. M. van Driel, *Appl. Phys. Lett.* **95**, 261910 (2009)
 - ³² J. J. Dean and H. M. van Driel, *Phys. Rev. B* **82**, 125411 (2010).
 - ³³ S. A. Mikhailov, *Phys. Rev. B* **84**, 045432 (2011).
 - ³⁴ M. M. Glazov, *JETP Lett.* **93**, 366 (2011).
 - ³⁵ D. A. Smirnova, I. V. Shadrivov, A. E. Miroshnichenko, A. I. Smirnov, and Y. S. Kivshar, *Phys. Rev. B* **90**, 035412 (2014).
 - ³⁶ X. Yao, M. Tokman, and A. Belyanin, *Phys. Rev. Lett.* **112**, 055501 (2014).
 - ³⁷ M. Tokman, Y. Wang, I. Oladyshkin, A. R. Kutayiah, and A. Belyanin, *Phys. Rev. B* **93**, 235422 (2016).
 - ³⁸ T. J. Constant, S. M. Hornett, D. E. Chang, and E. Hendry, *Nature Physics* **12**, 124 (2016).
 - ³⁹ H. Rostami, M. I. Katsnelson, M. Polini, *Phys. Rev. B* **95**, 035416 (2017).
 - ⁴⁰ L. E. Golub and S. A. Tarasenko, Valley polarization induced second harmonic generation in graphene, *Phys. Rev. B* **90**, 201402 (2014).
 - ⁴¹ T. O. Wehling, A. Huber, A. I. Lichtenstein, and M. I. Katsnelson, *Phys. Rev. B* **91**, 041404 (2015).
 - ⁴² Y. Wang, M. Tokman, A. Belyanin, *Phys. Rev. B* **94**, 195442 (2016).
 - ⁴³ J. L. Cheng, N. Vermeulen, J. E. Sipe, *Scientific reports* **7**, 43843 (2017).
 - ⁴⁴ Y. Zhang, D. Huang, Y. Shan, T. Jiang, Z. Zhang, K. Liu, L. Shi, J. Cheng, J. E. Sipe, W.-T. Liu, S. Wu, *Phys. Rev.*

- Lett. **122**, 047401 (2019).
- ⁴⁵ R. W. Boyd, *Nonlinear Optics* (Academic Press, San Diego, CA, (2003).
- ⁴⁶ K. J. Tielrooij, et al, *Nature Phys.* **9**, 248 (2013).